Front. Phys.
https://doi.org/10.15302/frontphys.2026.095208
CN 11-5994/O4
ISSN 2095-0462

RESEARCH ARTICLE

Dirac points and Weyl phase in a honeycomb altermagnet

Meng-Han Zhang[1], Xuan Guo[1], Dao-Xin Yao[1,2,*]

[1]State Key Laboratory of Optoelectronic Materials and Technologies, Center for Neutron Science and Technology, Guangdong Provincial Key Laboratory of Magnetoelectric Physics and Devices, School of Physics, Sun Yat-sen University, Guangzhou 510275, China

[2]International Quantum Academy, Shenzhen 518048, China

Received May 16, 2026; accepted May 22, 2026

We present unconventional nodal crossings in a two-dimensional collinear altermagnet, which are enforced by crystal symmetries to lock spin polarization and valley degrees of freedom. Altermagnetism generates nonrelativistic spin-splitting in honeycomb antiferromagnets, guaranteeing novel band degeneracies between bands sharing identical spin configurations yet different sublattices. Inspired by the XPS_3 (X=Mn, Fe, Ni) materials, we demonstrate distinctive Berry curvature distributions that are strongly concentrated near the Weyl nodes, which further generalize the locking between valleys and Berry curvature. Topological phase transitions are characterized by the high Chern numbers preserving the non-intersecting flows of Wannier centers over occupied bands, where degeneracy lifting contributes to unconventional spin textures to induce the valley Hall effect. Our results reveal unique topological nodes arising from the interplay between crystal symmetry constraints and intrinsic time-reversal symmetry breaking, whose associated topological responses are relevant for spintronic applications.

https://doi.org/10.15302/frontphys.2026.095208

RESEARCH ARTICLE

Dirac points and Weyl phase in a honeycomb altermagnet

Meng-Han Zhang,[1] Xuan Guo,[1] and Dao-Xin Yao[1,2,*]

[1]*State Key Laboratory of Optoelectronic Materials and Technologies, Center for Neutron Science and Technology, Guangdong Provincial Key Laboratory of Magnetoelectric Physics and Devices, School of Physics, Sun Yat-Sen University, Guangzhou 510275, China*

[2]*International Quantum Academy, Shenzhen 518048, China*

Received May 16, 2026; accepted May 22, 2026

We present unconventional nodal crossings in a two-dimensional collinear altermagnet, which are enforced by crystal symmetries to lock spin polarization and valley degrees of freedom. Altermagnetism generates non-relativistic spin-splitting in honeycomb antiferromagnets, guaranteeing novel band degeneracies between bands sharing identical spin configurations yet different sublattices. Inspired by the XPS_3 (X=Mn, Fe, Ni) materials, we demonstrate distinctive Berry curvature distributions that are strongly concentrated near the Weyl nodes, which further generalize the locking between valleys and Berry curvature. Topological phase transitions are characterized by the high Chern numbers preserving the non-intersecting flows of Wannier centers over occupied bands, where degeneracy lifting contributes to unconventional spin textures to induce the valley Hall effect. Our results reveal unique topological nodes arising from the interplay between crystal symmetry constraints and intrinsic time-reversal symmetry breaking, whose associated topological responses are relevant for spintronic applications.

I. INTRODUCTION

Two-dimensional (2D) honeycomb materials, including graphene and magnetic monolayers, exhibit unique electronic structures characterized by Dirac points and valley degrees of freedom. While extensive studies have focused on non-magnetic or weakly magnetic honeycomb lattices, the interplay between magnetism and topological band structures in collinear antiferromagnets remains less explored[1–3]. Recent experimental and theoretical studies have identified several transition-metal trichalcogenides, such as XPS_3 (X=Mn, Fe, Ni), as promising 2D honeycomb altermagnets[4–6]. In these systems, the combination of collinear magnetic order and honeycomb lattice symmetry gives rise to nontrivial electronic structures, which can be tuned by external parameters such as strain, electric field, or chemical substitution. First-principles calculations have revealed that these materials host symmetry-enforced band crossings and exhibit large Berry curvature near the high-symmetry points, suggesting that valley-contrasted topological transport phenomena could be realized experimentally[7–9].Moreover, the interplay between symmetry-breaking degeneracy lifting and sublattice-dependent spin textures provides a natural mechanism for the valley Hall effect without requiring strong spin-orbit coupling[10–12].

Members of the XPS_3 family share a monoclinic crystal structure with space group $C2/m$[13, 14], and their atomic positions have been precisely determined by x-ray diffraction on single crystals[15]. Despite this structural similarity, their magnetic configurations vary: $FePS_3$ exhibits an out-of-plane zigzag antiferromagnetic (AFM) order, $NiPS_3$ stabilizes an in-plane zigzag-AFM configuration, and $MnPS_3$ adopts a *Néel*-type AFM structure with out-of-plane magnetic moments at low temperatures[16–22]. Beyond the magnetic ordering itself, these compounds are further distinguished by their magnetic point groups, which impose symmetry constraints on the electronic band structures. Specifically, $FePS_3$ has a C_c2/m magnetic space group $NiPS_3$ is described by P_c2_1/m and P_s1 symmetries, and $MnPS_3$ corresponds to $C2'/m$ group[19–21]. These variations in magnetic symmetry, together with the interplay of crystal-field anisotropy and exchange interactions on the honeycomb lattice, play a crucial role in enforcing spin splitting, Dirac-like band crossings, and valley-dependent topological phenomena. Meanwhile, several theoretical and experimental studies have investigated the XPS_3 family in atomically thin limits[23]. Experiments have confirmed the persistence of magnetic order in $FePS_3$ and $NiPS_3$, providing a platform to probe 2D magnetism and the emergence of long-range order. Theoretical studies further suggest that $MnPS_3$ can serve as a symmetry-tunable antiferromagnetic substrate, capable of inducing and controlling spin and valley effects in 2D heterostructures without relying on net magnetization or strong spin-orbit coupling[22, 24]. Despite these advances, a comprehensive understanding of the microscopic mechanisms governing spin-lattice coupling, magnetic anisotropy, and symmetry-protected topological features across the XPS_3 family remains lacking, motivating further investigation.

Altermagnetic order, a recently recognized class of collinear magnetism, offers a unique platform for realizing spin-split Dirac and Weyl nodes. Unlike conventional ferromagnets (FMs) and antiferromagnets (AFMs), it breaks time-reversal symmetry while preserving vanishing net magnetization[7, 25–42]. We investigate the emergence of topological nodes within a tight-binding model formed by hexagonal clusters, where the altermagnetic order, rather than relativistic SOC, drives momentum-dependent spin splitting. By incorporating four-sublattice bond dimerization, we uncover symmetry-protected Weyl points that traverse high-symmetry lines in the first Brillouin zone and can merge or annihilate under the strong-weak bonds modulation. Although SOC is assumed to be negligible, it enables sig-

* Corresponding author:yaodaox@mail.sysu.edu.cn

nificant topological responses rather than incompatible with altermagnetism[43, 44], including the anomalous Hall effect (AHE) accompanied by emergent weak ferromagnetism. When integrated with proximity-induced superconductivity, the pairing symmetries and finite-momentum pairing in altermagnets offer fertile ground for researching novel topological phases and superconducting phenomena[45, 46].

Unconventional Zeeman splitting can induce diverse nontrivial topology in two-dimensional (2D) collinear antiferromagnets, while preserving symmetry-constrained zero net magnetization[47, 48]. By focusing on collinear antiferromagnetic order and crystal symmetries[49–51], we demonstrate Dirac cones and pairwise Weyl nodes in the honeycomb monolayer[52, 53]. The presence of these Dirac and Weyl nodes introduces valley degrees of freedom[54, 55], where the valley-polarized currents open additional avenues for manipulating electronic and spintronic properties in combination with intrinsic or induced spin polarization[56–59]. The coexistence of strong spin polarization and zero net magnetization endows altermagnet (AM) with both immunity to stray magnetic fields and the ability to support efficient spin-current generation[34, 57], establishing them as a versatile platform for exploring unconventional topological phases and spintronic applications[60–62].

In this work, we introduce a collinear altermagnetic order within 2D honeycomb lattice, which is characterized by dimerized bond strengths that from a four-sublattice superlattice structure. In Sec.II, we analyze the physical origin and symmetry basis of the Hamiltonian parameters. We further discuss the symmetry protection of our system and the evolution of Weyl points depending on hopping strengths and bond dimerization. In Sec.III, we examine the topological properties of the system, including the distribution of Berry curvature, and the formation of edge states in nanoribbons with zigzag and armchair terminations. In Sec.IV, we discuss experimental realizations and tunable platforms for altermagnetic topological phases, including electric-field control, strain engineering, ultracold atoms, and topolectrical circuits. Our results demonstrate the interplay between altermagnetic order and crystal symmetry, providing a versatile platform for generating valley-polarized currents and designing spintronics devices without relying on heavy-element SOC.

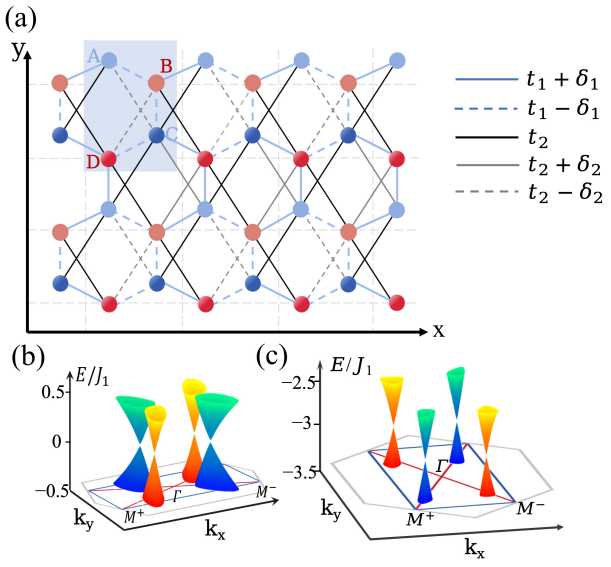

FIG. 1. (a) Schematic of the honeycomb-lattice model for altermagnetism. The model has four sublattices at each lattice point with red and blue dots denoting anti-aligned moments. The blue dashed lines represent the nearest-neighbor (NN) hopping strengths t_1-δ_1, and ellipses accompained with blue lines are hopping terms with negative signs t_1+δ_1. The crystalline environment generates anisotropic second-nearest-neighbor hopping (black solid and dashed lines) t_2 and δ_2. (b) Dirac crossings with spin-up and spin-down bands develop on the BZ edges. (c) Weyl points between bands of the same spin are shown in red and blue, respectively. The massless crossings along the high-symmetry directions $\Gamma - M$ annihilate each other into quadratic crossings.

II. MODEL AND METHODS

A. Magnetic Ground States

We investigate the XPS_3 (X = Fe, Ni, Mn) family of layered transition-metal phosphorus trichalcogenides, which display space group $C2/m$ as exemplary materials for 2D honeycomb lattice[63–65]. Our first-principles calculations are performed using density functional theory (DFT) with the four-state method to determine the magnetic ground state and extract exchange interactions[66, 67]. In this approach, four representative collinear spin configurations—ferromagnetic (FM) , AF-*Néel*, AF-zigzag, and AF-stripy—are considered, with lattice parameters fixed to those of the energetically most favorable configuration. By comparing the total energies of these configurations, we can identify the lowest-energy magnetic state objectively. We applied it to XPS_3 compounds, and the analytical expressions for the energies of collinear magnetic orders are employed

$$E_{\text{FM/Néel}} = E_0 + (\pm 3J_1 + 6J_2 \pm 3J_3)|S|^2, E_{\text{AF-zigzag/stripy}} = E_0 + (\pm J_1 - 2J_2 \mp 3J_3)|S|^2, \quad (1)$$

where E_0 is the spin-independent reference energy and S is the spin magnitude. Eventually, the computed DFT energies are mapped onto a classical Heisenberg Hamiltonian to extract exchange couplings J_1,J_2, and J_3, and the ground state is further verified via zero-temperature classical phase diagram analysis[68].

The point group and magnetic space group symmetries, along with the magnetic ground states determined from DFT calculations, are summarized in Table I. $MnPS_3$ stabilizes in the *N éel* state with the *N éel* vector aligned along the $\hat{z}$-direction, whereas $NiPS_3$ and $FePS_3$ favor the zigzag antiferromagnetic configuration. In $MnPS_3$, a *N éel*-type AFM structure with out-of-plane magnetic moments lowers the magnetic space group (MSG) to $C2'/m$. The zigzag-AFM configuration parallel to the plane is preserved in $NiPS_3$, where the space group and the MSG are transformed to P_c2_1/m

TABLE I. Structural data for the XPS_3 (X=Mn, Fe, Ni) materials.

Materials	$MnPS_3$	$FePS_3$	$NiPS_3$
Point Group magnetic	C_{2h}	C_{2h}	C_{2h}
space group Ground	$C2'/m$	$Cc2/m$	P_c2_1/m and P_s1
State $E_{\text{zigzag}}(eV)$	Néel	zigzag	zigzag
$E_{\text{Néel}}(eV)$	-436.22251799	-206.60581247	-189.04760342
$E_{\text{stripy}}(eV)$	-436.31236596	-206.58824763	-188.99952714
$(J_1, J_2, J_3)(meV)$	-436.24219519	-206.52173682	-188.65610965
	(0.482, 0.0413, 0.102)	(-1.50194, 0.27445, 3.00331)	(-3.55, -0.27, 15.13)

and P_s1 respectively. The table further lists the total energies for representative collinear spin configurations and the extracted exchange couplings (J_1, J_2, J_3), providing a comprehensive overview of the structural and magnetic properties of these monolayers. These distinct magnetic symmetries and spin configurations reflect the interplay between crystal field anisotropy and exchange interactions, establishing XPS_3 compounds as an ideal material platform for realizing and tuning 2D altermagnetism[69, 70].

B. Four-Sublattice Hamiltonian

We investigate the spectral properties of a modified honeycomb lattice as shown in fig. 1, manipulating the position and properties of the Dirac cones through hopping strengths. The cell-periodic Hamiltonian is given by

$$\begin{aligned} H_0(\boldsymbol{k}) = \tau_0 \otimes 2t_1 \Big[& \cos(k_1)\cos(k_2)\,\tau_x + \cos(k_1)\sin(k_2)\,\tau_y \Big] \\ & - \tau_z \otimes 2\delta_1 \Big[\sin(k_1)\sin(k_2)\,\tau_x - \sin(k_1)\cos(k_2)\,\tau_y \Big] \\ & + \tau_x \otimes t_1 \Big[\cos(2k_2)\,\tau_x - \sin(2k_2)\,\tau_y \Big] \\ & - \tau_y \otimes \delta_1 \Big[\sin(2k_2)\,\tau_x + \cos(2k_2)\,\tau_y \Big], \end{aligned} \tag{2}$$

where $\boldsymbol{k}_1 = \frac{\sqrt{3}}{2}\boldsymbol{k}_x$, $\boldsymbol{k}_2 = \frac{1}{2}\boldsymbol{k}_y$. We apply the model to a pristine hexagonal structure with the coupling between strong and weak nearest-neighbor bonds t_1 and δ_1, which leads to an enlargement of the unit cell and consequently reduces the size of the Brillouin zone. The original hexagonal Brillouin zone is reduced into a rectangular Brillouin zone, where the folding of electronic bands induces additional Van Hove singularities (vHSs) in the density of states (DOS) along high-symmetry lines. A bulk energy gap closes along the boundary of Brillouin zone (BZ) when $\delta_1 = 0$, exhibiting topologically protected linear crossings around the high-symmetry points $(\pm\frac{\pi}{\sqrt{3}}, 0)$. The dimerization of nearest-neighbor coupling breaks translational symmetry, introducing an anisotropic dispersion relation and altering the inherent topological characteristics. As depicted in Fig 2, the Dirac points that were initially pinned under rotational symmetry can move along the high-symmetry path, which undergo pairwise annihilation. The phase diagram delineates the transitions between trivial and topological semimetal phases and captures the critical localization of robust edge states.

We define the homeomorphism $R^1 \bigcup \infty \to S^1$ to illustrate tunable Dirac cones and phase transitions, where the vertical axis parameter is $\nu = \frac{\delta_1}{t_1}$ with a diameter of 5. As shown in Fig. 2, this mapping reveals a fundamental relation between the dimerization strength and the emergence of mass-less Dirac fermions. The Dirac cones unfold along a high-symmetry path for a set of NN hoppings, eventually merging into a semi-Dirac point characterized at critical values $\nu = 0, \pm\frac{\sqrt{5}}{5}, \pm\sqrt{5}$. Based on the conventional crystallographic setting of the monolayer XPS_3 in the C_{2h} point group symmetry, the dimerized bond strength forms a superlattice with an enlargement of the unit cell. We study the *Néel* order via antiparallel magnetic moments (μ=$M_A - M_B$=$M_C - M_D$) from the hopping of itinerant electrons, where the *Néel* vector is aligned along the $\hat{z}$-direction, resulting in $\mu\hat{z}$. As all rotational symmetries (C_{6z}, C_{3z}, C_{2z}) are broken, the system undergoes a symmetry reduction to the magnetic point group $C2/m$.

We analyze the transformation properties under point group $C2/m$ operations, where the origin of magnetic unit cell is situated at the midpoint of the strong bonds to naturally reflect the dimerization distribution. The positions of the four sites are $(0, \boldsymbol{k}_2)$, $(0, -\boldsymbol{k}_2)$, $(-\boldsymbol{k}_1, 2\boldsymbol{k}_2)$, and $(-\boldsymbol{k}_1, -2\boldsymbol{k}_2)$, respectively. Thus, the space of Bloch states is a 4-dimensional Hilbert space, and it is necessary to construct unitary gauge matrices to ensure the correct representation of symmetry operations.

$$\mathcal{U} = \begin{bmatrix} e^{i\boldsymbol{k}_2} & 0 & 0 & 0 \\ 0 & e^{-i\boldsymbol{k}_2} & 0 & 0 \\ 0 & 0 & e^{-i\boldsymbol{k}_1+2i\boldsymbol{k}_2} & 0 \\ 0 & 0 & 0 & e^{-i\boldsymbol{k}_1-2i\boldsymbol{k}_2} \end{bmatrix}. \tag{3}$$

The translation is still a lattice symmetry and preserves the four sublattice structure. With a half-translation via the (1/2, 1/2) lattice vector, an exchange occurs between sublat-tices A and C, as well as between sublattices B and D. The *Néel* order remains invariant under the product of this sublat-tice operation $\tau_x \otimes \tau_0$ and the non-symmorphic $\{E|\,\frac{1}{2}\}$. The half-translation operation $\{E|\,\frac{1}{2}\}$, as an integral component of the superlattice symmetry, imposes constraints that enforce degeneracy following band folding.

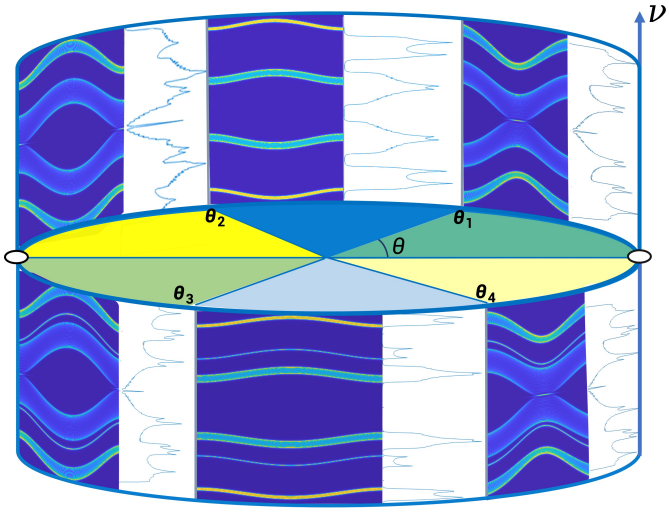

FIG. 2. Analytical demonstration of the phase diagram formed by ν and θ. The Dirac points merge together at the phase boundaries $\theta = \pm\arctan\frac{\sqrt{5}}{2}$ and $\pm(\pi-\arctan\frac{\sqrt{5}}{2})$, where the spectral function of edge modes and DOS are depicted for each separated phase.

C. Symmetries and Spectrum

We quantify the interaction strength between the itinerant electrons and the collinear local moments with staggered magnetization μ, constructing an altermagnetic model from the $\theta = \pi$ of S^1 at the critical point in Fig. 2. Within two decoupled subspaces, each possessing a well-defined spin, localized spins interact with itinerant electrons via a Kondo-like coupling of the form.

$$H_{AM}(\boldsymbol{k}) = \mu\tau_0 \otimes \tau_z. \tag{4}$$

By introducing the potential μ, we develop the Hamiltonian of the honeycomb lattice under collinear altermagnetic order, where the anisotropic next nearest-neighbor (nnn) hopping originates from distinct crystalline environments among the four sublattices. They are defined as operators $\boldsymbol{S}_1 = 2\delta_2 \sin(\boldsymbol{k}_1)\cos(3\boldsymbol{k}_2)\tau_y\otimes\tau_z$ and $\boldsymbol{S}_2 = -2\delta_2\cos(\boldsymbol{k}_1)\sin(3\boldsymbol{k}_2)\tau_y\otimes\tau_0$, where another term related to the NNN hopping t_2 is $\boldsymbol{S}_3 = 4t_2\cos(\boldsymbol{k}_1)\cos(3\boldsymbol{k}_2)\tau_x\otimes\tau_0$.

$$\begin{aligned} H(\boldsymbol{k}) &= \sigma_0 \otimes H_1(\boldsymbol{k}) + \sigma_z \otimes H_{AM}(\boldsymbol{k}), \\ H_1(\boldsymbol{k}) &= H_0(\boldsymbol{k}) + \boldsymbol{S}_1 + \boldsymbol{S}_2 + \boldsymbol{S}_3, \end{aligned} \tag{5}$$

where σ_i are Pauli matrices operating on the spin space. As the altermagnetic order explicitly breaks time-reversal symmetry $\mathcal{T} = -i\sigma_y K$, the quadratic energy spectrum becomes subject to the staggered potential that lifts the spin degeneracy. The energy spectrum with the staggered potential μ and NNN hoppings is obtained for the two spin-split altermagnetic subspaces as

$$E^{\pm} = \pm\mu \pm 2\sqrt{4t_2^2\cos^2(k_1)\cos^2(3k_2) + \delta_2^2\sin^2(k_1+3\pm k_2)}. \tag{6}$$

We perform a systematic analysis of the energy dispersion in the absence of SOC, where nodal line degeneracies arise exclusively from altermagnetic symmetries. The composite symmetry operator $\{\mathcal{T}C_{2z}|\frac{1}{2}\frac{1}{2}\}$ guarantees the Kramers degeneracy along the high-symmetry paths ($\Gamma - X$, $\Gamma - Y$, $M - X$, and $M-Y$), which combines time-reversal with a twofold rotation followed by a fractional lattice translation. Although mirror reflection transforms non-magnetic sites into their original positions, magnetic sites with two opposite-spin are mapped to each other with a spin-flip operation. Thus, the *Néel* vector undergoes sign reversal under mirror symmetry operation with $\tau_x \otimes \tau_x$, sharing identical symmetry characteristics with $\tau_0 \otimes \tau_z$. We examine the combination symmetries of $C_{2z}\mathcal{M}$ and $\mathcal{T}\mathcal{M}$, which stabilize the spin configurations contributing to the total magnetic moment compensation[71–74].

III. RESULTS

A. Weyl Nodes

When two electronic bands with identical spin polarization approach each other in momentum space, their crossing gives rise to Weyl nodes[50, 51]. Such degeneracy points require altermagnetic symmetry protection to maintain their topological stability, and their dispersion relations approach linear behavior. We consider an expansion of Hamiltonian around Weyl points into the subspace via the operator $\boldsymbol{P} = |\Psi^\alpha(\boldsymbol{k})\rangle\langle\Psi^\alpha(\boldsymbol{k})|\bigoplus|\Psi^\beta(\boldsymbol{k})\rangle\langle\Psi^\beta(\boldsymbol{k})|$.

$$\begin{aligned} H_{q^\alpha} &= \epsilon_q^\alpha\sigma_0 + v_y^\alpha q_x^\alpha\sigma_y \pm v_x^\alpha q_y^\alpha\sigma_x, \\ H_{q^\beta} &= \epsilon_q^\beta\sigma_0 + v_y^\beta q_x^\beta\sigma_y \pm v_x^\beta q_y^\beta\sigma_x, \end{aligned} \tag{7}$$

where $\epsilon_{\boldsymbol{q}}^\alpha$ and $\epsilon_{\boldsymbol{q}}^\beta$ denote the chemical potential in the vicinity of the Weyl nodes. Within the restricted subspace, the effective Hamiltonian can be expressed as a linear combination of Pauli matrices. The anisotropic velocities for spin-up subspace are v_x^α and v_y^α, where the counterparts for spin-down are represented by β. We derive the anisotropic velocities in the vicinity of pair-wise crossings $(\pm\frac{\pi}{\sqrt{3}}, \pm\frac{\pi-\arccos\sqrt{\xi}}{3})$.

$$\begin{aligned} v_y^\alpha &= v_y^\beta = \delta_2\sqrt{3\xi}, \\ v_x^{\alpha\beta} &= \sqrt{|9\delta_2^2 - 9R^2 \pm 18R^2\cos^4\frac{\sqrt{1-\xi}}{3}|}. \end{aligned} \tag{8}$$

where $\xi = |\frac{R^2}{2\delta_2^2} - 1|$, and $R^2 = t_1^2 + \mu^2$. We investigate the parity operator that maps a Weyl node to its counterpart, with spin and sublattice degrees of freedom treated independently. Acting as monopoles or anti-monopoles of Berry curvature, the gapped Weyl points enable the valley-dependent

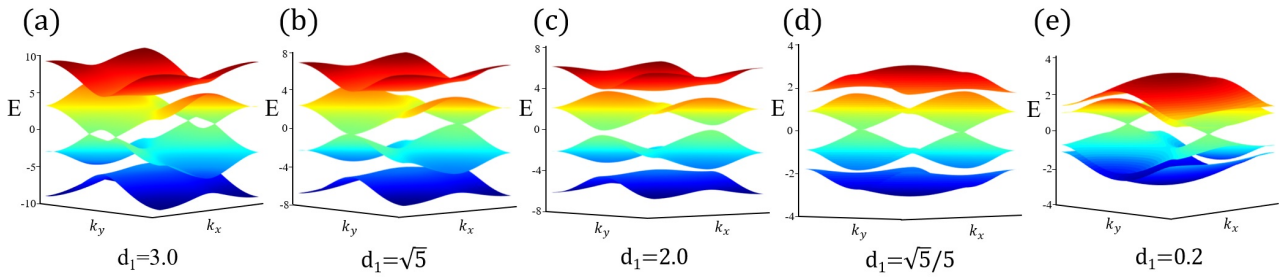

FIG. 3. The evolution of Dirac points in the bulk band structures across distinct phase regions of the phase diagram presented in Figure 2. (a) $\theta \in (0, \arctan\frac{\sqrt{5}}{2})$, (b) $\theta \in (\arctan\frac{\sqrt{5}}{2}, \pi - \arctan\frac{\sqrt{5}}{2})$, (c) $\theta \in (\pi - \arctan\frac{\sqrt{5}}{2}, \pi)$, (d) $\theta \in (0, -\arctan\frac{\sqrt{5}}{2})$, (e) $\theta \in (-\arctan\frac{\sqrt{5}}{2}, -\pi + \arctan\frac{\sqrt{5}}{2})$, (f) $\theta \in (-\pi + \arctan\frac{\sqrt{5}}{2}, -\pi)$.

Hall effect, chiral magnetic effects, and other exotic transport phenomena[75].

One potential approach to gap out the Weyl nodes is to apply the mass term $M_{\boldsymbol{k}} = m_1 \cos(2\boldsymbol{k}_1) + m_2 \sin(2\boldsymbol{k}_1)$, where m_1 and m_2 are coefficients, introduced by multiplying the general staggered hoppings with the operator $\tau_z \otimes \tau_0$. The **k**-dependent terms break the altermagnetic symmetries, and a functionally analogous effect can be achieved via the valley-selective coupling of circularly polarized light to electrons. The proposed mass terms can also originate from an intrinsic SOC of the Kane–Mele type, which is compatible with the symmetry of the spin angular momentum along the z direction. With a vanishing macroscopic magnetization, the symmetry of 2-fold spin rotation (C_{2z}) maintains the integrity under SO(2) transformation. For spin-1/2 fermions, the eigenvalues of the twofold rotation symmetries follow from the algebraic relation $C_{2z}^2 = -1$, which imposes a block-diagonal form on the Hamiltonian. This symmetry protects Weyl points along the high symmetry line $\Gamma - M$, where the band crossings are characterized by opposite rotation eigenvalues of $\pm i$. The topology of crossing is characterized by the Berry curvature $\Omega_{\pm}^{\alpha(\beta)}$

$$\begin{aligned}\Omega_{\pm}^{\alpha(\beta)} &= \frac{\boldsymbol{d}_{\boldsymbol{q}}^{\alpha(\beta)} \cdot [\partial_{q_x} \boldsymbol{d}_{\boldsymbol{q}}^{\alpha(\beta)} \times \partial_{q_y} \boldsymbol{d}_{\boldsymbol{q}}^{\alpha(\beta)}]}{|\boldsymbol{d}_{\boldsymbol{q}}^{\alpha(\beta)}|^3}, \\ &= \frac{|M_{\boldsymbol{k}}| v_x v_y}{2\sqrt[3]{v_x q_y^2 + v_y q_x^2 + M^2}},\end{aligned} \tag{9}$$

where $\boldsymbol{d}_{\boldsymbol{q}}^{\alpha(\beta)} = v_y^{\alpha(\beta)} \boldsymbol{q}_x + v_x^{\alpha(\beta)} \boldsymbol{q}_y + \frac{M_{\boldsymbol{k}}}{2} \boldsymbol{q}_z$. The distribution of Berry curvature contributes to the Berry Phase as

$$\Upsilon_{\pm}^{\alpha(\beta)} = \pm \frac{1}{4\pi} \int_{BZ} \Omega_{\pm}^{\alpha(\beta)} = \pm \frac{sgn(|M_{\boldsymbol{k}}|)}{2}, \tag{10}$$

where $|M_{\boldsymbol{k}}|$ is determined by the finite values of m_1 and m_2, lifting the degeneracy of crossings. The distribution of Berry curvature contributes to the total Hall current as $j = \frac{\hbar}{2e}(j^{\alpha} + j^{\beta}) = \frac{e^2}{\hbar} \mathcal{E} \sum^{\beta} sgn(M_{\boldsymbol{k}})$[76]. The parity operator $\mathcal{P}$: $(k_x, k_y) \rightarrow (-k_x, -k_y)$ indicates that band crossings evolve along the $\Gamma - M$ high-symmetry directions within a single spin sector. Considering the twofold rotation C_{2y} about y-axis, the system maintains mirror reflection passing across the vertical plane, described by $\mathcal{M}_y = \mathcal{P} C_{2y}$. Thus, the bands along high symmetry line exhibit at least twofold degeneracy for the out-of-plane *Néel* vector, which are preserved even when the mass term is introduced.

B. Phase Digram

The Weyl phase diagram is formed by t_2 and δ_2 in the configurational s pace fi xing $t_1 = 0$ an d $\delta_1 = 1$. We illustrate the evolution of Wannier centers obtained from the non-Abelian Berry phase in Fig. 5, corresponding to the integration of Berry connection with fully decoupled spin subspaces[77, 78]. The Wilson loop approach describes the evolution of Wannier centers based on the $U(2N)$ Berry connection $A^{\alpha\beta} = \langle \psi^{\alpha}(\boldsymbol{k}) | \psi^{\beta}(\boldsymbol{k} + \delta_{\boldsymbol{k}}) \rangle$. We project the $H_0(\boldsymbol{k})$ into the Bloch occupied states via the position operator $\sum_{\boldsymbol{k}} \sum_{\alpha,\beta=1}^{N_F} A^{\alpha\beta} |\Psi^{\beta}(\boldsymbol{k} + \delta_{\boldsymbol{k}})\rangle \langle \Psi^{\alpha}(\boldsymbol{k})|$. Typical phases are illustrated in Fig. 5, which are modified by varying the staggered magnetization as the control parameter. The Weyl crossings undergo a topological transition upon increasing the magnitude of the magnetization in altermagnets[79–81], enabling a variety of intriguing topological phenomena and anisotropic transport properties[76, 82, 83].

We present the band structure of the topological phase in a ribbon geometry, where midgap edge modes emerge distinctly. Each edge hosts a single spin-resolved mode, with spin-up and spin-down states explicitly labeled. Our numerical results demonstrate that increasing the SOC strength leads to a redistribution of the Berry curvature across the Brillouin zone, initially localized near the Weyl nodes. Despite this redistribution, the Chern number defined as the integral of the Berry curvature over the BZ remains invariant. Distinct Hall plateaus form whenever the chemical potential falls within this specific energy window. The emergence of a pronounced anomalous Hall effect under weak SOC is therefore both theoretically intriguing and experimentally accessible. For the 2D model with large μ values and an out-of-plane Néel vector, the topological edge modes emerge naturally with Chern bands. A distinct angular-dependent behavior in the anomalous Hall

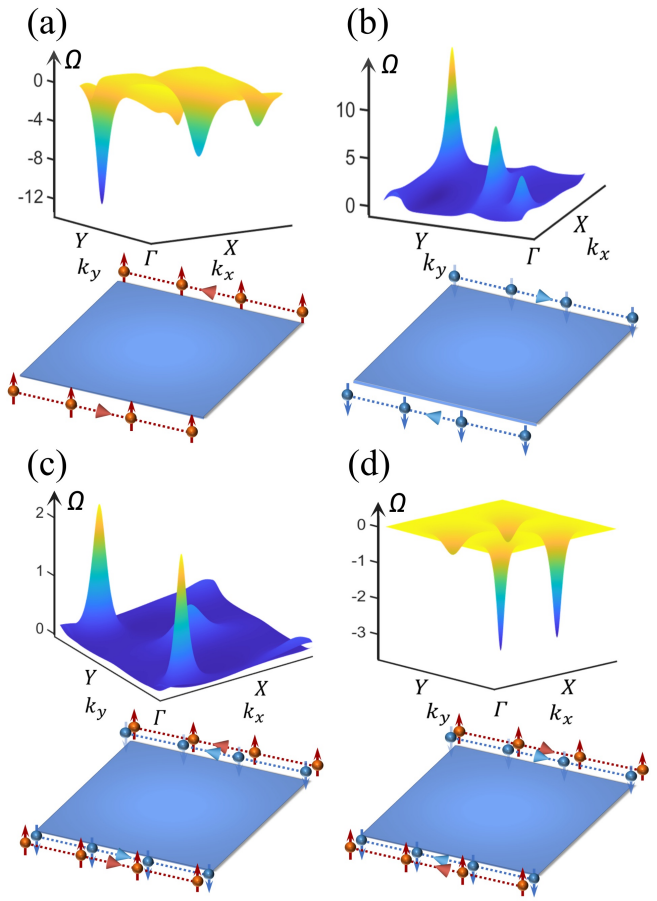

FIG. 4. The distribution of Berry curvature in the limit of $\nu \to \infty$. (a) The directions of spin-up edge currents with $C = 1$. We use the parameters $t_2 = 0.6$, $\delta_2 = 1.2$, $|\mu| = 0.6$, and set the coefficients of mass terms as $m_1 = 1$, m_2=1.3. (b) The directions of spin-down edge currents with C = -1. We use δ_2 = -1.2 setting the same other parameters as the former. (c) The spin-polarized current with $C = 2$. We use the parameters $t_2 = 0.6$, $\delta_2 = 1.2$, $|\mu| = 4$ fixing the mass term $m_2 = 0.3$. (d)The spin-polarized current with $C = -2$. We use $\delta_2 = -1.2$ with the same other parameters as the former.

effect provides a valuable supplementary approach for probing the band structure characteristics, offering complementary insights to conventional techniques like angle-resolved photoemission spectroscopy[76].

The spin degeneracy of the edge modes is lifted, allowing for unique chiral propagating states under the Z_2 topological classification[84]. We theoretically calculate the quantum Hall effect via the controlled fabrication of the valley degree of freedom in altermagnetic band structure in Fig. 5. The formation of Weyl points endows the spin-split band structure with nontrivial topology, where the Weyl nodes act as monopoles or antimonopoles of Berry curvature, with their charge determined by the chirality, as shown in Fig. 4. We depict the zigzag edges of altermagnetic ribbon, where the magnetic moments on adjacent sites are antiparallel. Induced by the antiparallel orientation of magnetic moments, the gap opening at the Weyl points illustrates chiral transport responses rather than helical spin textures[85, 86]. We propose that the injection of high-energy photons can induce nontrivial topological states in the altermagnetic model, in which the radiative recombination of spin-polarized carriers exhibits a finite net circular polarization[87]. These states can also be realized in non-Hermitian systems through the modulation of gain and loss, both of which are guided by mirror symmetry and PT symmetry[88].

IV. CONCLUSIONS

Exploring beyond monolayer XPS_3, two-dimensional honeycomb altermagnets have attracted increasing attention due to their unique low-energy physics governed by Dirac-like electronic dispersions. We consider a honeycomb lattice with engineered parameters to achieve bond dimerization and onsite potentials, exhibiting tunable edge states governed by their intrinsic topology. The mirror symmetry $\mathcal{M}$ remains the symmetry of bond-strength alternation, which is combined with time-reversal symmetry to ensure the symmetry compensation in altermagnets[89]. The antiparallel orientation of magnetic moments interacts differently with the up and down spin states, where spin splitting contributes to the formation of linear crossings with symmetry-protected degeneracies[90, 91]. Mandatory degeneracies occur along high-symmetry lines, which demonstrate the spin-splitting mode[52]. Enabling topologically quantized transport characteristics, our band structure calculations for various parameters reveal that mass terms can be identified as the gap-opening mechanism for Weyl points[60–62].

The application of an out-of-plane electric field can modulate magnetic interactions, driving the system toward more complex magnetic orderings[92, 93], while the nontrivial interplay of lattice symmetries suggests that $MnP(S, Se)_3$ can be functionalized from a two-dimensional antiferromagnet into a strong altermagnet[94]. The structural phase transition induced by chalcogen substitution modifies the exchange pathways, potentially creating the spin-split electronic bands characteristic of altermagnetic materials while preserving the compensated antiparallel spin configuration. The particular C_2 rotational symmetry of the Mn cation sublattice, combined with the ligand-field splitting induced by chalcogen substitution, creates the necessary conditions for alternating spin-polarized bands in both real and reciprocal spaces[95, 96]. These observations offer strong evidence for this unconventional magnetic ordering phenomenon. Combined with the Kerr effect, the polarized photons interacting with the staggered magnetic moments can regulate topological responses in advanced optoelectronic devices[97, 98].

Ultracold atoms in optical lattices provide a highly controllable platform for studying altermagnetic topology[99]. The precise manipulation of atomic interactions and lattice geometries enables the emulation of exotic quantum phases, including those exhibiting altermagnetic order with nontrivial band topology. By tuning the lattice parameters, we can engineer our model into different topological regimes via artificial mechanical lattices, allowing for the observation of the

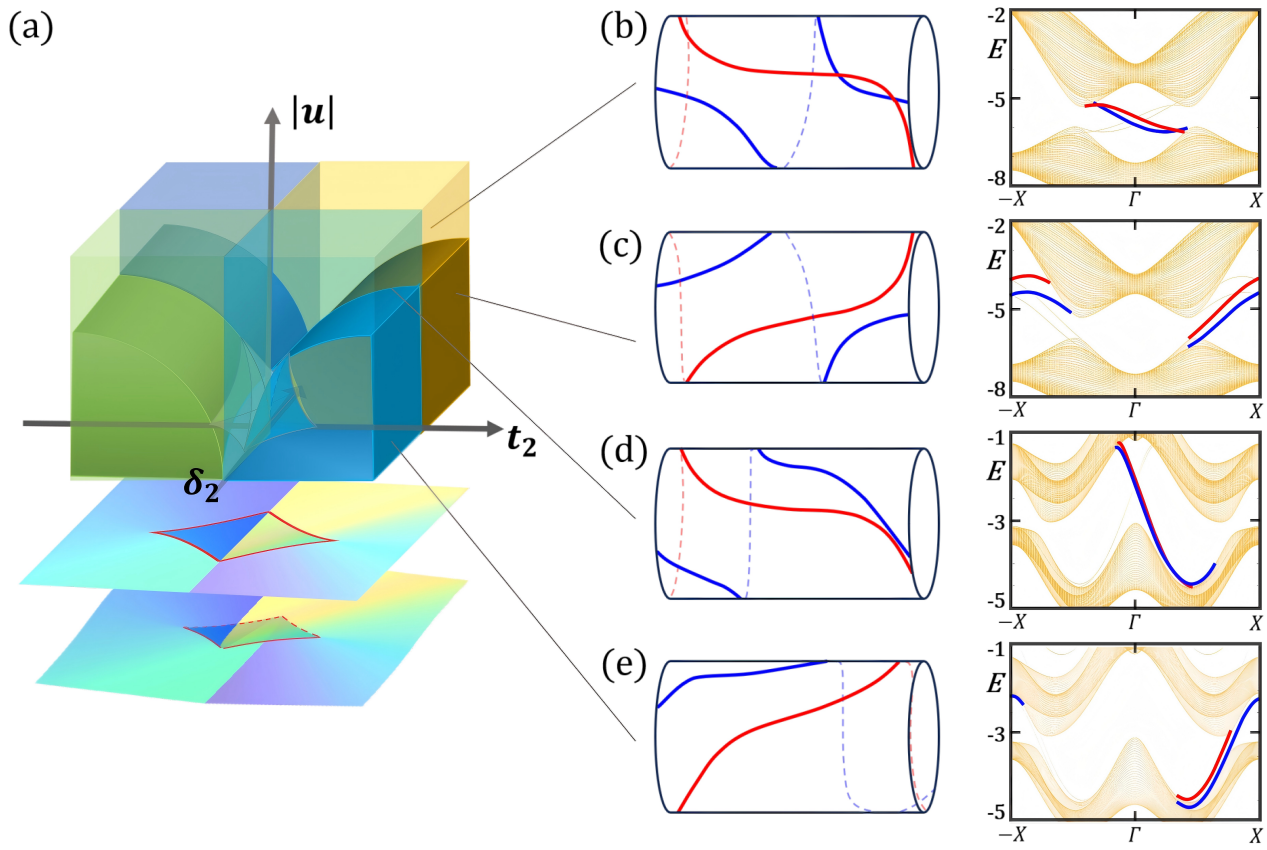

FIG. 5. (a) The Weyl phase diagram demonstrates the formation of Weyl points, where the phase boundary is related to the singularity class when the map sends regular values to critical values. The number of Weyl points in the vertical axis is determined by the staggered potential μ. (b)-(e) The curved surface separates the creation of weyl points from the gapped phase with $|\mu|$=0.6. The red line shows the chiral propagating states for spin-up, whereas the spin-down counterpart is in blue.

robust transport for chiral edge modes. Additionally, in ultracold atomic gases, the implementation of synthetic magnetic fields provides a controlled platform for engineering diverse topological phases and observing valley-dependent Hall effects[100, 101]. Topolectrical circuits hold promise for manipulating valley polarization through topological boundary resonances[102, 103], enabling selective excitation of valley-polarized states through appropriate impedance modulation. The valley-polarized modes demonstrate valley-contrasting transport properties, while the valley index provides an additional degree of freedom for information encoding[104–106]. Topolectrical circuits exploit the inherent degeneracy to engineer robust states that are immune to backscattering and disorder, enabling the realization of the valleytronic devices and the applications of topological quantum computing[107, 108].

ACKNOWLEDGMENTS

We thank Zi-Jian Xiong for helpful discussions. This project is supported by NKRDPC-2022YFA1402802, NSFC-92165204, NSFC-12494590, NSFC-92565303, Leading Talent Program of Guangdong Special Projects (201626003), Guangdong Provincial Key Laboratory of Magnetoelectric Physics and Devices (No.2022B1212010008), Research Center for Magnetoelectric Physics of Guangdong Province (2024B0303390001), and Guangdong Provincial Quantum Science Strategic Initiative (GDZX2401010).

Appendix A: Ribbon

Honeycomb structures are well known for their unique geometric and intricate textures, particularly their capabilities to support various topological states and modulation of electronic properties. We analyze the ribbon spectra across the phase diagram, with the persistence of edge states serving as evidence of their topological nature. Our Hamiltonian is formulated in momentum space as

$$\begin{bmatrix} 0 & h_0(\boldsymbol{k}) \\ h_0^\dagger(\boldsymbol{k}) & 0 \end{bmatrix}, \tag{A1}$$

where $h_0(\boldsymbol{k})$ denotes a 2×2 block matrix expressed in the transformed basis $\psi_{\mathbf{k}} = (c_{\mathbf{k},A}, c_{\mathbf{k},C}, c_{\mathbf{k},B}, c_{\mathbf{k},D})^T$. The particular basis transformation arises from applying the sym-

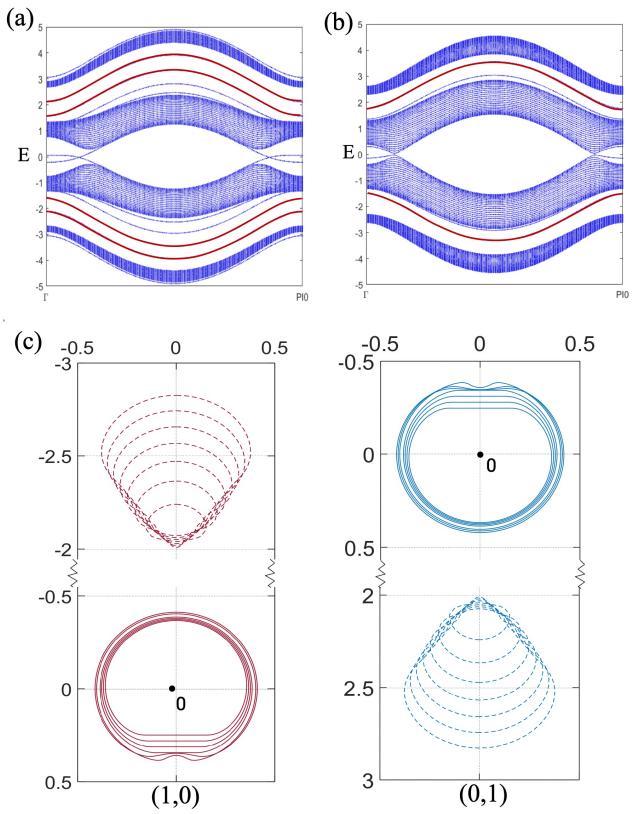

FIG. 6. (a) The band structures are calculated for the zigzag-terminated interface separating two topological domains characterized by opposite signs of δ_1. (b) Degenerate edge states of zigzag ribbons under uniform mass term. (c) Two pairs of winding numbers for even and odd parity. The parameters of ν are chosed at equal intervals from -1.2 to 1.2.

metry operation $\tau_x \otimes \tau_x$ to the original four sublattices, which performs the mapping $(c_{\mathbf{k},A}, c_{\mathbf{k},C}, c_{\mathbf{k},B}, c_{\mathbf{k},D})^T = \tau_x \otimes \tau_x (c_{\mathbf{k},A}, c_{\mathbf{k},B}, c_{\mathbf{k},C}, c_{\mathbf{k},D})^T$. This approach proves particularly valuable for examining the features of related topological boundary states. We investigate the sublattice symmetry in this Hamiltonian with chiral operator $\chi = \tau_0 \otimes \tau_z$, defining the $h_0(\boldsymbol{k})$ as

$$t_1 \begin{bmatrix} (1-\nu)e^{i\boldsymbol{a}_1} + (1+\nu)e^{-i\boldsymbol{a}_2} & (1+\nu)e^{2ik_2} \\ (1-\nu)e^{-2ik_2} & (1-\nu)e^{-i\boldsymbol{a}_2} + (1+\nu)e^{i\boldsymbol{a}_1} \end{bmatrix}, \quad \text{(A2)}$$

where $\boldsymbol{a}_1 = \boldsymbol{k}_1 - \boldsymbol{k}_2$ and $\boldsymbol{a}_2 = \boldsymbol{k}_1 + \boldsymbol{k}_2$. The corresponding energy dispersion relations take the form $E_0(\boldsymbol{k}) = \pm t_1 \sqrt{\Lambda(\boldsymbol{k}) \pm 2\sqrt{\lambda(\boldsymbol{k})}}$, where two $\pm$ signs distinguish the particle-hole symmetric branches corresponding to conduction and valence bands.

$$\begin{aligned} \Lambda(\boldsymbol{k}) &= 1 + 4\cos^2(k_1) + \nu^2\left[1 + 4\sin^2(k_1)\right], \\ \lambda(\boldsymbol{k}) &= \left[\cos^2(3k_2) + \nu^2\sin^2(3k_2)\right]\left[4\cos^2(k_1) + 4\nu^2\sin^2(k_1)\right] \\ &\quad + \nu^2. \end{aligned} \quad \text{(A3)}$$

We preserve the propagation direction of robust edge conduction, especially at interfaces, which originates in the two-dimensional Su-Schrieffer-Heeger (SSH) model for polymers[109–111]. As shown in fig. 3, the topological nodes move towards $(\pm\frac{1}{\sqrt{3}}\arccos\frac{\nu^2+3}{2\nu^2-2}, \frac{\pi}{3})$ and eventually merge together, transforming the semimetallic state into an insulating state with the gap size $2\sqrt{1+5\nu^2-2\nu\sqrt{5}}$. Fig. 6 presents the ribbon spectrum with zigzag termination for the parameters $t_1 = 0.5$ and $\delta_1 = -1.5$ in the presence of on-site energies of magnitude 1 associated with $\tau_x \otimes \tau_0$, where the edge modes persist regardless of the on-site energy amplitudes. We further examine the influence of boundary effects on edge potentials in nontrivial ribbons, with assigned parameters of 0.5 for the initial hexagonal cell and -0.2 for the last hexagonal cell. Breaking inversion symmetry lifts the degeneracy of the edge modes, whose robustness is controlled primarily by $|\delta_1|$ rather than by the SOC strength, in sharp contrast to conventional topological insulators.

We present the energy spectrum and the density of states (DOS) of the edge modes in Fig. 2, while their spatial distributions are depicted under the open boundary condition with 30 units in the perpendicular direction. At the critical point indicated in Fig. 2, the t_1 term opens the altermagnetic nodal line generating the spin-polarized Dirac cones with $\delta_1 = 0$. The nanoribbon spectrum supports localized edge states that span the whole zigzag terminations with pronounced van Hove singularities (vHSs), while the armchair configurations exhibit more uniform band structures rather than sharp spikes in the DOS[112]. We align two nanoribbons with complementary bond patterns to ensure effective overlap of the edge states, thereby promoting efficient state mobility dynamically via geometric or bond modulation[113–115]. Dimerization strengths and specific perturbations can drive the formation and unfolding of Dirac cones, which are crucial for developing next-generation transistors and sensors that leverage high mobility and unique electronic properties[116]. The resulting convergence of Dirac cones gives rise to highly anisotropic electronic properties, whereby direction-dependent dispersions strongly affect transport responses, conductivity, and the density of states near the Fermi level.

Appendix B: Winding number

Chiral symmetry proves particularly valuable for examining the features of related topological boundary states, where the eigenvalue associated with the chiral symmetry operator for a zero-energy state exhibits a direct correspondence with the winding number. Our study of chiral symmetry uncovers intriguing electronic wave function properties, which display distinct features governed by winding numbers. The wave functions can be classified into even- and odd-parity subspaces relative to chiral symmetry, which are effectively described by winding numbers.

$$w^\chi = \frac{1}{2\pi i}\int d\boldsymbol{k}\frac{d}{d\boldsymbol{k}}\log h_0^\chi(\boldsymbol{k}), \quad \text{(B1)}$$

where the winding number is derived as a topological invariant by fixing $k_2 = 0$ for zigzag edges and $k_1 = 0$ for arm-

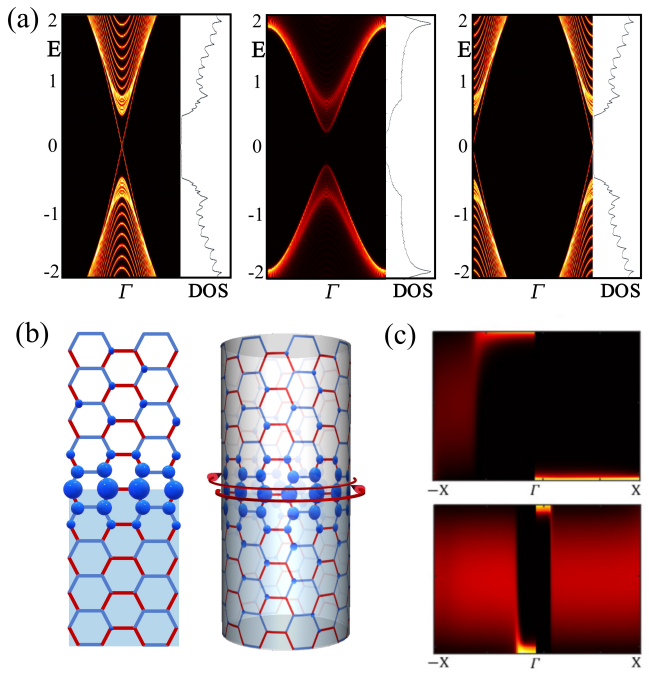

FIG. 7. (a) Armchair edge modes periodic along k_1 are regarded as a ribbon on a cylinder, where the amplitude of wave function is localized in the interface. (b) The energy spectrums correspond to the propagating edge modes with armchair-terminated interface, which indicate $(1,-1)$ for $\nu > 0$ and $(0,0)$ for $\nu < 0$. (c) Localized edge modes exhibit linear dispersion for the counterpropagating edge states.

chair terminations. The $h_0(\boldsymbol{k}_1)$ is diagonalized with the chiral operator χ to yield the expression

$$h_0^{\chi}(\boldsymbol{k}_1) = e^{-ik_1} + 1 + \chi\sqrt{\nu^2(e^{-ik_1}-1)^2 - \nu^2 + 1}. \qquad \text{(B2)}$$

Exploring the chiral symmetry in the presence of zigzag edges reveals unique characteristics of the electronic wave functions defined by winding numbers, within the subspaces of even and odd parity. The disparity in δ_1 values originates from variations in hopping strengths, enabling the formation of domain boundaries between different regions quantized by the sign function $sgn(W)$. When regions with opposing δ_1 values are interfaced for zigzag ribbons, $(1,0)$ and $(0,1)$ distinctly identify two topological phases in Fig. 6. Localized boundary states emerge at the interface due to the difference in winding numbers, determining the total winding number to classify the phases of the wave function in different regions. The development of real-space textures leverages zero-energy states that are topologically protected by chiral symmetry and localized at the edges, where a sign reversal in the winding number induces a concomitant sign flip in the eigenvalue. Bond dimerization modulates the band structure by inducing an energy gap, alternating hopping strengths between adjacent sites. The opening of the energy gap shifts the electronic behavior from massless Dirac fermions to a gapped state, endowing electrons with an effective mass. The corresponding spin textures are derived by meticulously analyzing the wave functions, enabling manipulation of topological edge states influenced by the hopping energy within these structures.

When open boundary conditions are imposed along the k_2 direction, the wave-vector component k_1 can be treated as a parameter. Fig. 7 depicts a decorated armchair ribbon terminated by vacuum together with its corresponding band structure, where distinct counterpropagating edge modes emerge for $\delta_1 < 0$. The topological boundary states are subsequently determined by examining the topological characteristics of this effective one-dimensional Hamiltonian. The chiral operator anticommutes with the Hamiltonian, reflecting the fundamental symmetry constraint on the system. The winding number exhibits two distinct nontrivial values, namely $+1$ and -1, demonstrating that chiral symmetry offers a richer topological characterization of surface states compared to single-parameter systems. The presence of these two quantized winding numbers implies that chiral-symmetric systems possess a more nuanced topological classification scheme for edge states. As chiral symmetry is a nonspatial symmetry, the zero-energy states simultaneously serve as eigenstates of the chiral symmetry operator, rendering their spin textures straightforward to determine. The electronic spectrum observed along armchair edges in the $\boldsymbol{k}_2$ direction reveals localized edge states at the vacuum interface, which is topologically guaranteed by nonzero winding number $(1,-1)$ with inherent robustness against perturbations.

[1] A. H. Castro Neto, F. Guinea, N. M. R. Peres, K. S. Novoselov, and A. K. Geim, The electronic properties of graphene, Reviews of Modern Physics **81**, 109 (2009).

[2] J. Wang, S. Deng, Z. Liu, and Z. Liu, The rare two-dimensional materials with dirac cones, National Science Review **2**, 22 (2015).

[3] S. Li, Y. Liu, Z.-M. Yu, Y. Jiao, S. Guan, X.-L. Sheng, Y. Yao, and S. A. Yang, Two-dimensional antiferromagnetic dirac fermions in monolayer tacote$_2$, Physical Review B **100**, 205102 (2019).

[4] J.-U. Lee and et al., Ising-type magnetic ordering in atomically thin feps3, Nano Letters **16**, 7433 (2016).

[5] M. Gibertini, M. Koperski, A. F. Morpurgo, and K. S. Novoselov, Magnetic 2d materials and heterostructures, Nature Nanotechnology **14**, 408 (2019).

[6] L. Smejkal, J. Sinova, and T. Jungwirth, Emerging research landscape of altermagnetism, Physical Review X **12**, 040501 (2022).

[7] R. Tamang, S. Gurung, S. R. Bhandari, M. J. Stitz, G. Pokharel, K. Shrestha, and D. Rai, A first-principles investigation of altermagnetism in crsb2 under applied pressure, arXiv preprint arXiv:2506.13454 (2025).

[8] S. Yan, Y. Du, X. Zhang, X. Wan, and D. Wang, First-principles study of magnetic interactions and excitations in

antiferromagnetic van der waals material mpx3 (m= mn, fe, co, ni; x= s, se), Journal of Physics: Condensed Matter **36**, 065502 (2024).
[9] P. Li, X. Li, J. Feng, J. Ni, Z.-X. Guo, and H. Xiang, Origin of zigzag antiferromagnetic order in x ps 3 (x= fe, ni) monolayers, Physical Review B **109**, 214418 (2024).
[10] L. Šmejkal, J. Sinova, and T. Jungwirth, Emerging research landscape of altermagnetism, Physical Review X **12**, 040501 (2022).
[11] S. Hayami, Y. Yanagi, and H. Kusunose, Momentum-dependent spin splitting by collinear antiferromagnetic ordering, journal of the physical society of japan **88**, 123702 (2019).
[12] D.-F. Shao, S.-H. Zhang, M. Li, C.-B. Eom, and E. Y. Tsymbal, Spin-neutral currents for spintronics, Nature Communications **12**, 7061 (2021).
[13] A. R. Wildes, V. Simonet, E. Ressouche, G. J. Mcintyre, M. Avdeev, E. Suard, S. A. Kimber, D. Lançon, G. Pepe, B. Moubaraki, *et al.*, Magnetic structure of the quasi-two-dimensional antiferromagnet nips 3, Physical Review B **92**, 224408 (2015).
[14] C. Li, Z. Hu, X. Hou, S. Xu, Z. Wu, K. Du, S. Li, X. Xu, Y. Chen, Z. Wang, *et al.*, Molecular intercalation in the van der waals antiferromagnets feps 3 and nips 3, Physical Review B **109**, 184407 (2024).
[15] G. Ouvrard, R. Brec, and J. Rouxel, Structural determination of some mps3 layered phases (m= mn, fe, co, ni and cd), Materials research bulletin **20**, 1181 (1985).
[16] T. Olsen, Magnetic anisotropy and exchange interactions of two-dimensional feps3, nips3 and mnps3 from first principles calculations, Journal of Physics D: Applied Physics **54**, 314001 (2021).
[17] J. Peng and X. Tong, Structural and magnetic properties of van der waals layered metal phosphorous trichalcogenides, physica status solidi (b) **262**, 2400517 (2025).
[18] R. Basnet, K. M. Kotur, M. Rybak, C. Stephenson, S. Bishop, C. Autieri, M. Birowska, and J. Hu, Controlling magnetic exchange and anisotropy by nonmagnetic ligand substitution in layered mpx 3 (m= ni, mn; x= s, se), Physical Review Research **4**, 023256 (2022).
[19] D. Lançon, H. Walker, E. Ressouche, B. Ouladdiaf, K. Rule, G. McIntyre, T. Hicks, H. M. Rønnow, and A. Wildes, Magnetic structure and magnon dynamics of the quasi-two-dimensional antiferromagnet feps 3, Physical Review B **94**, 214407 (2016).
[20] R. Ballou, Magnetoelectric $mnps_3$ as a candidate for ferrotoroidicity, Physical Review B **82**, 100408 (2010).
[21] A. Wildes, J. Stewart, M. Le, R. Ewings, K. Rule, G. Deng, and K. Anand, Magnetic dynamics of nips 3, Physical Review B **106**, 174422 (2022).
[22] K. Wrzos, M. Birowska, and M. Rybak, Symmetry-breaking phenomena in mnps3/tmdc heterostructures: Non-relativistic spin splitting, altermagnetism and spin-valley effects, arXiv preprint arXiv:2511.22209 (2025).
[23] C.-Y. Cheon, V. Multian, K. Watanabe, T. Taniguchi, A. F. Morpurgo, and D. Lebedev, Nature of 2d xy antiferromagnetism in a van der waals monolayer, Nature Communications (2025).
[24] R. Kumar and J.-G. Park, van der waals antiferromagnets: From early discoveries to future directions in the 2d limit, Journal of Magnetism and Magnetic Materials , 173977 (2026).
[25] L. Smejkal, R. González-Hernández, T. Jungwirth, and J. Sinova, Crystal time-reversal symmetry breaking and spontaneous hall effect in collinear antiferromagnets, Science Advances **6**, eaaz8809 (2020).
[26] S. Hayami, Y. Yanagi, and H. Kusunose, Momentum-dependent spin splitting by collinear antiferromagnetic ordering, Journal of the Physical Society of Japan **88**, 123702 (2019).
[27] S. Hayami, Y. Yanagi, and H. Kusunose, Bottom-up design of spin-split and reshaped electronic band structures in antiferromagnets without spin-orbit coupling: Procedure on the basis of augmented multipoles, Physical Review B **102**, 144441 (2020).
[28] L.-D. Yuan, Z. Wang, J.-W. Luo, E. I. Rashba, and A. Zunger, Giant momentum-dependent spin splitting in centrosymmetric low-z antiferromagnets, Physical Review B **102**, 014422 (2020).
[29] L.-D. Yuan, Z. Wang, J.-W. Luo, and A. Zunger, Prediction of low-z collinear and noncollinear antiferromagnetic compounds having momentum-dependent spin splitting even without spin-orbit coupling, Physical Review Materials **5**, 014409 (2021).
[30] I. I. Mazin, K. Koepernik, M. D. Johannes, R. Gonzalez-Hernández, and L. Smejkal, Prediction of unconventional magnetism in doped fesb2, Proceedings of the National Academy of Sciences **118**, e2108924118 (2021).
[31] D.-F. Shao, S.-H. Zhang, M. Li, C.-B. Eom, and E. Y. Tsymbal, Spin-neutral currents for spintronics, Nature Communications **12**, 7061 (2021).
[32] H.-Y. Ma, M. Hu, N. Li, J. Liu, W. Yao, J.-F. Jia, and J. Liu, Multifunctional antiferromagnetic materials with giant piezomagnetism and noncollinear spin current, Nature Communications **12**, 2846 (2021).
[33] P. Liu, J. Li, J. Han, X. Wan, and Q. Liu, Spin-group symmetry in magnetic materials with negligible spin-orbit coupling, Physical Review X **12**, 021016 (2022).
[34] Z. Feng, X. Zhou, L. Smejkal, L. Wu, Z. Zhu, H. Guo, R. Gonzalez-Hernández, X. Wang, H. Yan, P. Qin, X. Zhang, H. Wu, H. Chen, Z. Meng, L. Liu, Z. Xia, J. Sinova, T. Jungwirth, and Z. Liu, An anomalous hall effect in altermagnetic ruthenium dioxide, Nature Electronics **5**, 735 (2022).
[35] R. D. Gonzalez Betancourt, J. Zubač, R. Gonzalez-Hernandez, K. Geishendorf, Z. Sobán, G. Springholz, K. Olejník, L. Smejkal, J. Sinova, T. Jungwirth, S. T. B. Goennenwein, A. Thomas, H. Reichlova, J. Železný, and D. Kriegner, Spontaneous anomalous hall effect arising from an unconventional compensated magnetic phase in a semiconductor, Physical Review Letters **130**, 036702 (2023).
[36] I. I. Mazin, Altermagnetism in mnte: Origin, predicted manifestations, and routes to detwinning, Physical Review B **107**, L100418 (2023).
[37] I. Turek, Altermagnetism and magnetic groups with pseudoscalar electron spin, Physical Review B **106**, 094432 (2022).
[38] A. Hariki, T. Yamaguchi, D. Kriegner, K. W. Edmonds, P. Wadley, S. S. Dhesi, G. Springholz, L. Smejkal, K. Výborný, T. Jungwirth, and J. Kunes, X-ray magnetic circular dichroism in altermagnetic α-mnte, arXiv:2305.03588 (2023).
[39] S. Bhowal and N. A. Spaldin, Ferroically ordered magnetic octupoles in d-wave altermagnets, Physical Review X **14**, 011019 (2024).
[40] X. Zhou, W. Feng, R.-W. Zhang, L. Smejkal, J. Sinova, Y. Mokrousov, and Y. Yao, Crystal thermal transport in altermagnetic ruo2, Physical Review Letters **132**, 056701 (2024).
[41] L. Bai, W. Feng, S. Liu, L. Šmejkal, Y. Mokrousov, and Y. Yao, Altermagnetism: Exploring new frontiers in magnetism and spintronics, Advanced Functional Materials **34**,

2409327 (2024).
[42] S. Zeng, D. Liu, H. Peng, C.-C. He, X.-B. Yang, and Y.-J. Zhao, Classification and design of two-dimensional altermagnets, Front. Phys. 21, 095301 (2026).
[43] L. Šmejkal, J. Sinova, and T. Jungwirth, Beyond conventional ferromagnetism and antiferromagnetism: A phase with nonrelativistic spin and crystal rotation symmetry, Phys. Rev. X **12**, 031042 (2022).
[44] L. Fu and C. L. Kane, Topological insulators with inversion symmetry, Phys. Rev. B **76**, 045302 (2007).
[45] S.-B. Zhang, L.-H. Hu, and T. Neupert, Finite-momentum cooper pairing in proximitized altermagnets, Nature Communications **15**, 1801 (2024).
[46] D. Zhu, Z.-Y. Zhuang, Z. Wu, and Z. Yan, Topological superconductivity in two-dimensional altermagnetic metals, Phys. Rev. B **108**, 184505 (2023).
[47] L.-D. Yuan, Z. Wang, J.-W. Luo, E. I. Rashba, and A. Zunger, Giant momentum-dependent spin splitting in centrosymmetric low-z antiferromagnets, Phys. Rev. B **102**, 014422 (2020).
[48] L. Šmejkal, J. Sinova, and T. Jungwirth, Emerging research landscape of altermagnetism, Phys. Rev. X **12**, 040501 (2022).
[49] C. Li, M. Hu, Z. Li, Y. Wang, W. Chen, B. Thiagarajan, M. Leandersson, C. Polley, T. Kim, H. Liu, C. Fulga, M. G. Vergniory, O. Janson, O. Tjernberg, and J. van den Brink, Topological weyl altermagnetism in CrSb, arXiv , 2405.14777 (2024).
[50] S. Liu, C. Wang, L. Liu, J.-H. Choi, H.-J. Kim, Y. Jia, C. H. Park, and J.-H. Cho, Ferromagnetic weyl fermions in two-dimensional layered electride Gd_2C, Phys. Rev. Lett. **125**, 187203 (2020).
[51] K. Parshukov, R. Wiedmann, and A. P. Schnyder, Topological responses from gapped weyl points in 2d altermagnets, arXiv , 2403.09520 (2024).
[52] S. Bhowal and N. A. Spaldin, Ferroically ordered magnetic octupoles in d-wave altermagnets, Phys. Rev. X **14**, 011019 (2024).
[53] J. Ding, Z. Jiang, X. Chen, Z. Tao, Z. Liu, T. Li, J. Liu, J. Sun, J. Cheng, J. Liu, Y. Yang, R. Zhang, L. Deng, W. Jing, Y. Huang, Y. Shi, M. Ye, S. Qiao, Y. Wang, Y. Guo, D. Feng, and D. Shen, Large band-splitting in g-wave type altermagnet crsb, Physical Review Letters **133** (2024).
[54] M. Ezawa, Detecting the néel vector of altermagnets in heterostructures with a topological insulator and a crystalline valley-edge insulator, Phys. Rev. B **109**, 245306 (2024).
[55] Y.-Q. Li, W.-Y. Tong, and C.-G. Duan, Altermagnetic ferrovalley materials: Paradigm shift and frontier advances in valleytronics, Front. Phys. **21**, 075302 (2026).
[56] J. Zhou, Q. Sun, and P. Jena, Valley-polarized quantum anomalous hall effect in ferrimagnetic honeycomb lattices, Physical Review Letters **119**, 046403 (2017).
[57] L. Šmejkal, Y. Mokrousov, B. Yan, and A. H. MacDonald, Topological antiferromagnetic spintronics, Nature Physics **14**, 242 (2018).
[58] K. F. Mak, K. L. McGill, J. Park, and P. L. McEuen, The valley hall effect in mos_2 transistors, Science **344**, 1489 (2014).
[59] C. Luo, Z. Huang, H. Qiao, X. Qi, and X. Peng, Valleytronics in two-dimensional magnetic materials, Journal of Physics: Materials **7**, 022006 (2024).
[60] S. Bhowal and N. A. Spaldin, Ferroically ordered magnetic octupoles in d-wave altermagnets, Physical Review X **14**, 011019 (2024).
[61] R. Gonzalez Betancourt, J. Zubáč, R. Gonzalez-Hernandez, K. Geishendorf, Z. Šobáň, G. Springholz, K. Olejník, L. Šmejkal, J. Sinova, T. Jungwirth, *et al.*, Spontaneous anomalous hall effect arising from an unconventional compensated magnetic phase in a semiconductor, Physical Review Letters **130**, 036702 (2023).
[62] P. H. Fu, Q. Lv, Y. Xu, J. Cayao, J. F. Liu, and X. L. Yu, All-electrically controlled spintronics in altermagnetic heterostructures, npj Quantum Materials **10**, 111 (2025).
[63] I. Turek, Altermagnetism and magnetic groups with pseudoscalar electron spin, Phys. Rev. B **106**, 094432 (2022).
[64] S. Zeng and Y.-J. Zhao, Description of two-dimensional altermagnetism: Categorization using spin group theory, Phys. Rev. B **110**, 054406 (2024).
[65] P. Liu, J. Li, J. Han, X. Wan, and Q. Liu, Spin-group symmetry in magnetic materials with negligible spin-orbit coupling, Phys. Rev. X **12**, 021016 (2022).
[66] G. Wan, Y. Li, T. Lai, P. Li, Y. Zhu, J. Yang, Y.-F. Zhang, J. Pan, and S. Du, Sym4state. jl: An efficient computation package for magnetic materials, Computer Physics Communications **303**, 109283 (2024).
[67] C. Xu, B. Xu, B. Dupé, and L. Bellaiche, Magnetic interactions in bifeo 3: A first-principles study, Physical Review B **99**, 104420 (2019).
[68] T. Y. Kim and C.-H. Park, Magnetic anisotropy and magnetic ordering of transition-metal phosphorus trisulfides, Nano Letters **21**, 10114 (2021).
[69] H. Ma, M. Hu, N. Li, J. Liu, W. Yao, J.-F. Jia, and J. Liu, Multifunctional antiferromagnetic materials with giant piezomagnetism and noncollinear spin current, Nature Communications **12**, 2846 (2021).
[70] Y.-L. Lee, Magnetic impurities in an altermagnetic metal, arXiv , 2312.15733 (2023).
[71] L. Šmejkal, J. Sinova, and T. Jungwirth, Beyond conventional ferromagnetism and antiferromagnetism: A phase with nonrelativistic spin and crystal rotation symmetry, Physical Review X **12**, 031042 (2022).
[72] L. Šmejkal, J. Sinova, and T. Jungwirth, Emerging research landscape of altermagnetism, Physical Review X **12**, 040501 (2022).
[73] I. Turek, Altermagnetism and magnetic groups with pseudoscalar electron spin, Physical Review B **106**, 094432 (2022).
[74] S.-W. Cheong and F.-T. Huang, Altermagnetism classification, npj Quantum Materials **10**, 38 (2025).
[75] X. Chen, D. Wang, L. Li, and B. Sanyal, Giant spin-splitting and tunable spin-momentum locked transport in room temperature collinear antiferromagnetic semimetallic cro monolayer, Applied Physics Letters **123**, 022402 (2023).
[76] X.-L. Qi, Y.-S. Wu, and S.-C. Zhang, Topological quantization of the spin hall effect in two-dimensional paramagnetic semiconductors, Phys. Rev. B **74**, 085308 (2006).
[77] A. Yamamoto, Berry phase in lattice qcd, Phys. Rev. Lett. **117**, 052001 (2016).
[78] D. Xiao, M.-C. Chang, and Q. Niu, Berry phase effects on electronic properties, Rev. Mod. Phys. **82**, 1959 (2010).
[79] J. Nag, B. Das, S. Bhowal, Y. Nishioka, B. Bandyopadhyay, S. Sarker, S. Kumar, K. Kuroda, V. Gopalan, A. Kimura, K. G. Suresh, and A. Alam, Gdalsi: An antiferromagnetic topological weyl semimetal with non-relativistic spin splitting, arXiv , 2312.11980 (2024).
[80] R. Soto-Garrido, E. Muñoz, and V. Juričić, Dislocation defect as a bulk probe of monopole charge of multi-weyl semimetals, Phys. Rev. Res. **2**, 012043 (2020).
[81] L. Del Re, Dirac points and topological phases in correlated altermagnets, Phys. Rev. Research **7**, 033234 (2025).
[82] L. Šmejkal, A. H. MacDonald, J. Sinova, S. Nakatsuji, and T. Jungwirth, Anomalous hall antiferromagnets, Nature Re-

views Materials **7**, 482 (2022).
[83] Z. Feng, Z. X., S. L., W. L., Z. Zhu, G. H., G.-H. R. a., X. Wang, and Y. H., An anomalous hall effect in altermagnetic ruthenium dioxide, Nature Electronics **5**, 735–743 (2022).
[84] J.-W. Rhim, J. Behrends, and J. H. Bardarson, Bulk-boundary correspondence from the intercellular zak phase, Phys. Rev. B **95**, 035421 (2017).
[85] L. Šmejkal, R. González-Hernández, T. Jungwirth, and J. Sinova, Crystal time-reversal symmetry breaking and spontaneous hall effect in collinear antiferromagnets, Science Advances **6**, eaaz8809 (2020).
[86] R. Hoyer, R. Jaeschke-Ubiergo, K.-H. Ahn, L. Šmejkal, and A. Mook, Spontaneous crystal thermal hall effect in insulating altermagnets, arXiv , 2405.05090 (2024).
[87] J. Wang, X. Chen, B.-F. Zhu, and S.-C. Zhang, Topological *p-n* junction, Phys. Rev. B **85**, 235131 (2012).
[88] A. F. Young and P. Kim, Quantum interference and klein tunnelling in graphene heterojunctions, Nature Physics **5**, 222 (2009).
[89] R.-J. Slager, A. Mesaros, V. Juričić, and J. Zaanen, Interplay between electronic topology and crystal symmetry: Dislocation-line modes in topological band insulators, Phys. Rev. B **90**, 241403 (2014).
[90] O. Fedchenko, J. Minár, A. Akashdeep, S. W. D'Souza, D. Vasilyev, O. Tkach, L. Odenbreit, Q. Nguyen, D. Kutnyakhov, N. Wind, *et al.*, Observation of time-reversal symmetry breaking in the band structure of altermagnetic ruo$_2$, Sci. Adv. **10**, eadj4883 (2024).
[91] D. S. Antonenko, R. M. Fernandes, and J. W. F. Venderbos, Mirror chern bands and weyl nodal loops in altermagnets, Phys. Rev. Lett. **134**, 096703 (2025).
[92] A. Hariki, A. Dal Din, O. J. Amin, T. Yamaguchi, A. Badura, D. Kriegner, K. W. Edmonds, R. P. Campion, P. Wadley, D. Backes, L. S. I. Veiga, S. S. Dhesi, G. Springholz, L. Šmejkal, K. Výborný, T. Jungwirth, and J. Kuneš, X-ray magnetic circular dichroism in altermagnetic α-mnte, Phys. Rev. Lett. **132**, 176701 (2024).
[93] S. Lee, S. Lee, S. Jung, J. Jung, D. Kim, Y. Lee, B. Seok, J. Kim, B. G. Park, L. Šmejkal, C.-J. Kang, and C. Kim, Broken kramers degeneracy in altermagnetic mnte, Phys. Rev. Lett. **132**, 036702 (2024).
[94] I. Mazin, R. González-Hernández, and L. Šmejkal, Induced monolayer altermagnetism in mnp(s,se)3 and fese, arXiv , 2309.02355 (2023).
[95] C.-C. Wei, X. Li, S. Hatt, X. Huai, J. Liu, B. Singh, K.-M. Kim, R. M. Fernandes, P. Cardon, L. Zhao, T. T. Tran, B. M. Frandsen, K. S. Burch, F. Liu, and H. Ji, $La_2o_3mn_2se_2$: a correlated insulating layered d-wave altermagnet, arXiv , 2410.14542 (2024).
[96] M. Ezawa, Third-order and fifth-order nonlinear spin-current generation in *g*-wave and *i*-wave altermagnets and perfect spin-current diode based on *f*-wave magnets, arXiv , 2411.16036 (2024).
[97] M. Eschbach, E. Młyńczak, J. Kellner, J. Kampmeier, M. Lanius, E. Neumann, C. Weyrich, M. Gehlmann, P. Gospodarič, S. Döring, G. Mussler, and N. Demarina, Realization of a vertical topological p–n junction in epitaxial sb2te3/bi2te3 heterostructures, Nature Communications **6**, 8816 (2015).
[98] R. Ilan, F. de Juan, and J. E. Moore, Spin-based mach-zehnder interferometry in topological insulator *p*–*n* junctions, Phys. Rev. Lett. **115**, 096802 (2015).
[99] P. Das, V. Leeb, J. Knolle, and M. Knap, Realizing altermagnetism in fermi-hubbard models with ultracold atoms, Phys. Rev. Lett. **132**, 263402 (2024).
[100] X. Zhai and Y. M. Blanter, Topological valley transport of gapped dirac magnons in bilayer ferromagnetic insulators, Phys. Rev. B **102**, 075407 (2020).
[101] D. Xiao, W. Yao, and Q. Niu, Valley-contrasting physics in graphene: Magnetic moment and topological transport, Phys. Rev. Lett. **99**, 236809 (2007).
[102] Y. Huang and X. Chen, Quantum circuit complexity of one-dimensional topological phases, Phys. Rev. B **91**, 195143 (2015).
[103] J. Ningyuan, C. Owens, A. Sommer, D. Schuster, and J. Simon, Time- and site-resolved dynamics in a topological circuit, Phys. Rev. X **5**, 021031 (2015).
[104] C. H. Lee, S. Imhof, C. Berger, F. Bayer, J. Brehm, L. W. Molenkamp, T. Kiessling, and R. Thomale, Topolectrical circuits, Communications Physics **1**, 39 (2018).
[105] A. Paler, I. Polian, K. Nemoto, and S. J. Devitt, Fault-tolerant, high-level quantum circuits: form, compilation and description, Quantum Science and Technology **2**, 025003 (2017).
[106] A. Paler, A. G. Fowler, and R. Wille, Synthesis of arbitrary quantum circuits to topological assembly: Systematic, online and compact, Scientific Reports **7**, 10414 (2017).
[107] A. Paler, S. J. Devitt, K. Nemoto, and I. Polian, Mapping of topological quantum circuits to physical hardware, Scientific Reports **4**, 4657 (2014).
[108] P. Roushan, C. Neill, Y. Chen, M. Kolodrubetz, C. Quintana, N. Leung, M. Fang, R. Barends, B. Campbell, Z. Chen, B. Chiaro, A. Dunsworth, E. Jeffrey, J. Kelly, A. Megrant, and J. Mutus, Observation of topological transitions in interacting quantum circuits, Nature **515**, 241 (2014).
[109] F. Liu and K. Wakabayashi, Novel topological phase with a zero berry curvature, Phys. Rev. Lett. **118**, 076803 (2017).
[110] S. Jeon and Y. Kim, Two-dimensional weak topological insulators in inversion-symmetric crystals, Phys. Rev. B **105**, L121101 (2022).
[111] J. K. Asbóth, L. Oroszlány, and A. Pályi, The su–schrieffer–heeger (ssh) model, in *A Short Course on Topological Insulators: Band Structure and Edge States in One and Two Dimensions* (Springer, 2016) pp. 1–22.
[112] Y. Yu, H.-G. Suh, M. Roig, and D. F. Agterberg, Altermagnetism from coincident van hove singularities: application to κ-cl, arXiv , 2402.05180 (2024).
[113] A. H. Castro Neto, F. Guinea, N. M. R. Peres, K. S. Novoselov, and A. K. Geim, The electronic properties of graphene, Rev. Mod. Phys. **81**, 109 (2009).
[114] Y. Jiang, Z. Song, T. Zhu, Z. Fang, H. Weng, Z.-X. Liu, J. Yang, and C. Fang, Enumeration of spin-space groups: Toward a complete description of symmetries of magnetic orders, Phys. Rev. X **14**, 031039 (2024).
[115] W. F. Brinkman, R. J. Elliott, and R. E. Peierls, Theory of spin-space groups, Proceedings of the Royal Society of London. Series A. Mathematical and Physical Sciences **294**, 343 (1966).
[116] G. van Miert and C. Ortix, Dislocation charges reveal two-dimensional topological crystalline invariants, Phys. Rev. B **97**, 201111 (2018).